ARTICLE

Check for updates

Determining the temperature of a millikelvin scanning tunnelling microscope junction

Taner Esat [1,2], Xiaosheng Yang [1,2], Farhad Mustafayev[1,2], Helmut Soltner [3], F. Stefan Tautz [1,2,4] & Ruslan Temirov [1,5✉]

Cooling the junction of a scanning tunneling microscope to millikelvin temperatures is fundamental for high-resolution scanning tunneling spectroscopy. However, accurately determining the junction temperature has proven elusive, due to the microscopic dimension of the junction and its continuous energy exchange with the surrounding environment. Here, we employ a millikelvin scanning tunnelling microscope cooled by an adiabatic demagnetization refrigerator. Using normal-metal and superconducting tips, we perform scanning tunnelling spectroscopy on an atomically clean surface of Al(100) in a superconducting state. By varying the refrigerator temperatures between 30 mK and 1.2 K, we show that the temperature of the junction is decoupled from the temperature of the surrounding environment. To corroborate our findings, we simulate the scanning tunnelling spectroscopy data with $P(E)$ theory and determine that the junction has a temperature of 77 mK, despite its environment being at 1.5 K.

[1] Peter Grünberg Institut (PGI-3), Forschungszentrum Jülich, 52425 Jülich, Germany. [2] Jülich Aachen Research Alliance (JARA), Fundamentals of Future Information Technology, 52425 Jülich, Germany. [3] Zentralinstitut für Engineering, Elektronik und Analytik (ZEA-1), Forschungszentrum Jülich, 52425 Jülich, Germany. [4] Experimentalphysik IV A, RWTH Aachen University, 52074 Aachen, Germany. [5] Institute of Physics II, Faculty of Mathematics and Natural Sciences, University of Cologne, 50937 Cologne, Germany. ✉email: r.temirov@fz-juelich.de

The quantum effect of electron tunneling lies at the heart of scanning tunneling microscopy (STM). STM junctions operated in a highly controlled manner under ultra-high vacuum (UHV) and low-temperature conditions enable high-resolution imaging, and precise manipulation of surface nanostructures[1]. However, further explorations of quantum-coherent phenomena in such nanostructures[2] may demand even better control over the STM junction and its environment because of the utmost sensitivity of quantum tunneling to the microscopic properties of the tunneling junction and its environment. Since the temperature is one of the most critical environmental parameters, STM setups operating at ultra-low temperatures, i.e., well below 1 K, are being developed[3–13].

The motivation for conquering the millikelvin (mK) temperature range with STM is two-fold: First, the ultra-low temperatures stabilize emergent quantum ground states with exceptional properties[14–16]. Second, upon cooling the junction, the width of the Fermi–Dirac distribution in its electrodes shrinks, increasing the energy resolution of scanning tunneling spectroscopy (STS) and, in that way, also providing better access to low-energy excitations with longer lifetimes[17–19].

The problem of determining and later controlling the STM junction temperature is, however, anything but trivial. The most straightforward reason is that a direct temperature measurement typically performed with macroscopic sensors is technically impossible in such a microscopic junction. Another complication is that the junction permanently exchanges energy with its environment. These energy exchange processes affect the tunneling rates appreciably[20], requiring the characterization of the environmental temperature, too.

One indirect way of deducing the junction temperature is to perform an STS experiment, i.e., to measure the dependence of the tunneling current I on the applied bias voltage V. Most generally,

$$I = e[\Gamma^+(V) - \Gamma^-(V)], \quad (1)$$

where e is the elementary charge and $\Gamma^\pm$ is the tunneling rate in the direction along (against) the applied bias voltage. For an STM junction interacting with its electromagnetic environment[20], Γ^+ can be calculated from

$$\Gamma^+(V) = \frac{4\pi}{\hbar} \iint_{-\infty}^{\infty} dEdE' n_T(E) n_S(E' + eV) f_T(E)$$
$$\times [1 - f_S(E' + eV)] |M(E, E' + eV)|^2 P(E - E'), \quad (2)$$

where $n_{T,S}$ are the densities of states (DOS) and $f_{T,S}(E) = 1/[1 + \exp(E/k_B T_{T,S})]$ are the Fermi–Dirac distribution functions of the tip (T) and sample (S) electrodes. k_B is the Boltzmann constant and M is Bardeen's matrix element accounting for the overlap between the single-electron wavefunctions in the tip and the sample[21–23]. Apart from the last factor under the integral, Eq. (2) is identical to the classical result by Bardeen for the tunneling current in a junction isolated from the environment and connected to an ideal voltage source[20,21].

The environment enters Eq. (2) in the form of the so-called $P(E)$ function, which describes the probability for the tunneling electron to exchange the energy E with the environment[20]. $P(E - E')$ substitutes the delta function $\delta(E - E')$ in Bardeen's original expression for the non-interacting junction, thus accounting for the fact that also inelastic tunneling processes occur. Note that it is the thermal dependence of $f_{T,S}(E)$ that allows extracting the temperature of the tip T_T and the sample T_S from the STS data if $n_{T,S}(E)$ and $P(E)$ are known.

The problem with $n_{T,S}(E)$ is that it generally results from a complicated and often irregular atomic structure of the tip or sample, respectively. For evaluating $T_{T,S}$, it is therefore desirable to use materials with a well-defined DOS, on which atomic defects have little influence. Viable candidates to this aim are the Bardeen–Cooper–Schrieffer (BCS) superconductors with their DOS given by the well-known expression[24]

$$n^{BCS}(E) = n_0 Re \left[\frac{1}{\sqrt{E^2 - \Delta^2}} \right], \quad (3)$$

in which n_0 defines the DOS in the normal state and Δ is the halfwidth of the superconducting gap. n^{BCS} features two spectroscopic singularities—the so-called quasiparticle peaks—situated symmetrically around E_F at the lowest quasiparticle excitation energy $\pm\Delta$. Since according to Eq. (3) the quasiparticle peaks are spectroscopically very sharp, the effect of their temperature-dependent broadening can help the accurate evaluation of $T_{T,S}$ in a mK STM junction.

In a tunneling junction comprising a normal metal tip and a superconducting surface, when the temperature is substantially lower than the critical temperature of the superconducting transition T_c, Eq. (2) for $\Gamma^+(V)$ simplifies to

$$\Gamma^+(V) = \frac{1}{e^2 R} \iint_{-\infty}^{\infty} dEdE' n_S^{BCS}(E' + eV)$$
$$\times f_T(E) P(E - E'), \quad (4)$$

losing its dependence on $f_S(E)$ and hence T_S. Also note that under the assumption $n_T(E) = \text{const}$, and $M(E, E') = \text{const}$, in the relevant range of energies, they factor out and together with n_0 are absorbed into R, the high bias, or normal-state resistance of the junction. According to Eq. (4), tunneling between a normal metal tip and a superconducting surface yields T_T if the $P(E)$ function is known. Conversely, tunneling between a superconducting tip and a normal metal surface yields T_S. Interestingly, in a junction with both electrodes being superconducting the tunneling current, i.e., the Josephson current of Cooper pairs, is completely independent of $T_{T,S}$ if $T_{T,S} \ll T_c$, and is given by

$$I(V) = \frac{\pi e E_J}{\hbar} [P(2eV) - P(-2eV)], \quad (5)$$

which thus provides the most direct way of determining the $P(E)$ function experimentally[20]. In Eq. (5), $E_J = \hbar I_c/2e$ is the Josephson energy and I_c the critical Josephson current.

The first attempt at determining $P(E)$ of an STM junction is due to Ast and coworkers[25,26]. Applying the $P(E)$ theory as sketched in the "Methods" section, they successfully simulated the experimental STS data collected with a dilution-refrigerator-operated mK STM[5] on various tunneling junctions[25–31]. They also demonstrated that the $P(E)$ function causes broadening of the STS data and thus imposes a fundamental limitation on the resolution of STS experiments. Furthermore they proposed that the effective capacitance of the STM junction C is an important factor determining the degree of that broadening[26].

Up to now, $P(E)$ theory has been applied to STM, under the assumption that the junction is well thermalized with its environment, or in other words, the temperature of the junction is equal to that of its environment: $T_{T,S} = T_{env}$. It is, however, possible to envision a situation where this condition does not hold[32,33].

Here we demonstrate that the junction of our mK STM is much colder than the surrounding environment $T_T \ll T_{env}$ by performing variable-temperature STS of the Al(100) surface in its superconducting state, using both normal-metal and superconducting STM tips. First, we measured the temperature-dependent Josephson conductance and recovered the $P(E)$ function of the environment together with its temperature T_{env} from these data. Then we employed the obtained $P(E)$ function and T_{env} for evaluating the temperature T_T of the STM tip, which we consider to be an upper estimate of the junction temperature. Specifically, we obtained T_T
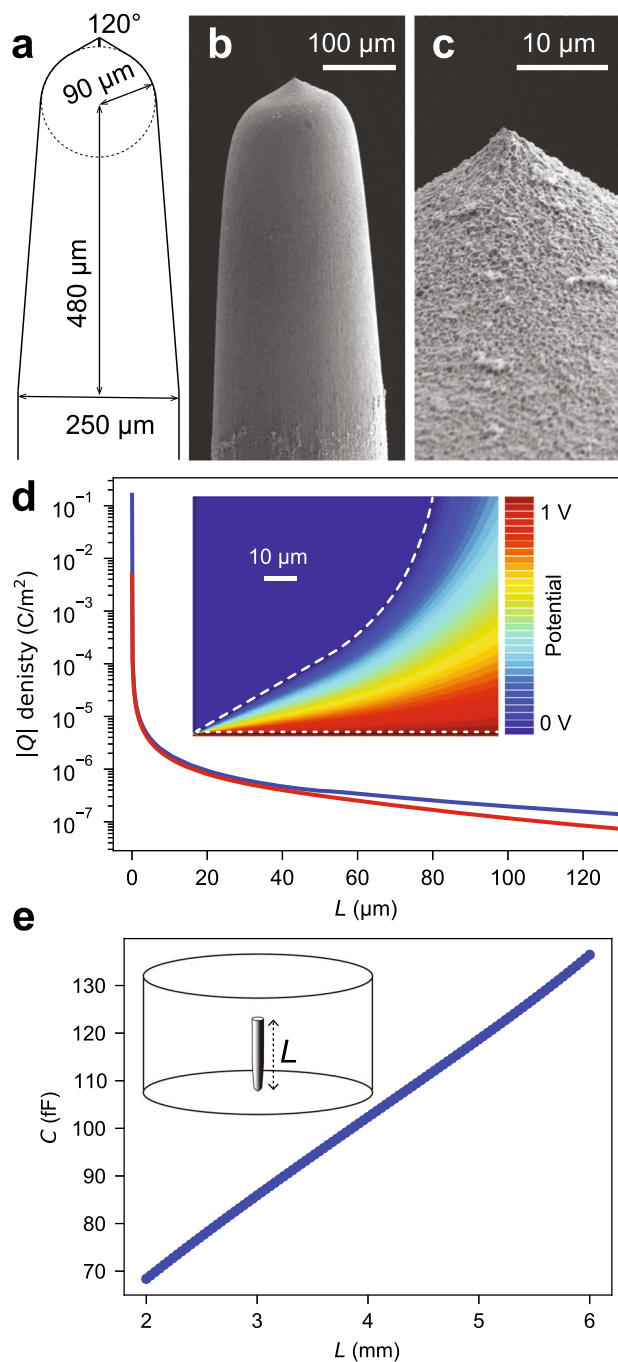
Fig. 1 Capacitance of the scanning tunneling microscope (STM) junction.
a Model of the tip based on the scanning electron microscope (SEM)
images (**b**, **c**). **b**, **c** SEM images of the tip. **d** Simulated surface charge
density in the junction biased by the voltage of 1 V. Distribution of the
potential in the junction (inset). The dashed white lines represent the
outline of the tip and the sample. **e** Dependence of the junction capacitance
C on the length L of the tip wire. Model of the STM head used for simulating
C (inset).

by fitting the STS of the superconducting gap measured with a
normal metal tip. In doing so, we additionally expose a potential
problem of the commonly used fitting approach and suggest how to
avoid it. Finally, we argue that the comparatively warm environ-
ment of our mK STM junction results in photon-assisted tunneling
that is responsible for the in-gap conductance seen in the STS of the
superconducting gap.

Results and discussion

Capacitance of the tip-sample junction. Considering the
broadening effect of the tip-sample junction capacitance C on
STS[26], we attempted to increase C by using blunter PtIr tips. The
model of the tip geometry exhibited in Fig. 1a was extracted from
the scanning electron microscopy images shown in Fig. 1b, c: We
approximated the tip apex shape by a sphere 90 μm in radius and
crowned by a cone with 120° opening angle.

Placing the model tip over a flat metal surface, we simulated
the charge distribution in the tip-sample junction with a
commercial software employing the boundary element method
(BEM)[12]. Figure 1d shows the simulated surface charge resulting
from a potential difference of 1 V applied to the sample while the
grounded tip is located at a distance of 1 nm. Although the
induced charge density drops quickly with the distance from the
tip apex, a more careful analysis shows that the density of charge
that accumulates on the shaft of the tip, i.e., far from the apex, is
not negligible.

Because the energy resolution of a mK STM may be as high as
10 μeV which corresponds to ≈2.5 GHz[11], the dimensions
contributing to the junction capacitance may reach the scale of
several cm. We, therefore, considered the complete STM head[12]
for evaluating C. A simplified model that captures the essential
features of our miniature[12] STM head (Fig. 1e) pictures the
junction capacitor as a cylindrical metallic cavity with a radius of
7 mm and a height of 7 mm inside which the tip, i.e., the second
electrode, is located. The bottom of the cavity coincides with the
surface plane of the sample; hence, the distance from the tip to
the cavity bottom is 1 nm. Systematically changing the length of
the tip wire L between 2 and 6 mm, we obtained the plot shown
in Fig. 1e, which demonstrates that C depends on L and hence the
correct evaluation of C needs to account for such additional
elements as the tip holder and possibly also the tunneling current
wire connected to the tip. Instead of performing more elaborate
simulations, we pick $C = 100$ fF as a ballpark value for our
analysis and later show that the picture that emerges from this
analysis does not qualitatively change upon reasonably limited
variations of C.

Temperature of the environment. According to $P(E)$ theory, the
environment of the STM junction is essentially the source of the
fluctuations of the junction's phase $\tilde{\phi}$ (see Eq. (9) in the Methods
section), which couple to the charge degree of freedom Q of the
junction and thus affect the tunneling process. The fluctuation-
dissipation theorem enables one to represent the fluctuating
environment by a dissipative impedance R_{env} connected in series
to the tunneling junction with resistance R and capacitance C as
shown in the lumped element model[20] in Fig. 2. Because the
spectrum of fluctuations depends on the temperature T_{env} of the
environment (see Eq. (10)), an analysis of experimental tunneling
spectra yields the value of T_{env}[32]. As was mentioned in the
introduction, Josephson tunneling spectroscopy provides the
most direct access to the $P(E)$ function of the environment and
hence T_{env}.

We exploited the unique capability of our instrument to
perform temperature-dependent STS and recorded 91 differential
conductance $dI/dV(V)$ spectra of the STM junction in the
Josephson regime while increasing the temperature T_{ADR} of the
adiabatic demagnetization refrigerator from 34 to 600 mK. The
spectra were acquired automatically with a rate of one spectrum
per every 30 min. The measurement was done on an atomically
clean superconducting Al(100) surface using a superconducting
tip. The latter was prepared by gentle indentations of the PtIr tip
(see Fig. 1) into the Al(100) surface. Visual inspection of the
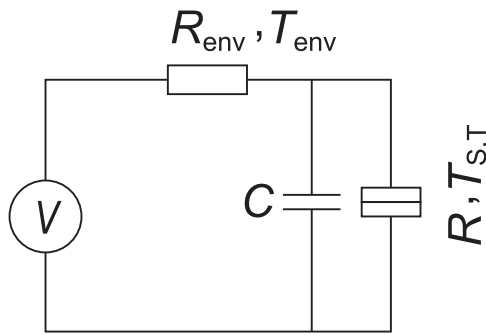spectra in Fig. 3 reveals that the Josephson conductance peak,

Fig. 2 Lumped element circuit model of the scanning tunneling microscope (STM) junction and its environment. The tunneling junction with tunneling resistance R and temperature $T_{S,T}$ is shunted by the junction capacitance C and connected to a purely dissipative impedance R_{env} whose temperature is T_{env}.

located at zero bias[20] and visible in all spectra up to $T_{ADR} \approx 500$ mK, shows no noticeable thermal dependence, except for its eventual disappearance above 500 mK, which most likely is a natural consequence of the loss of superconductivity in the tip. This finding is surprising, considering that T_{ADR} experiences an almost 20-fold increase.

In an attempt to rationalize the absence of the thermal dependence in the data, we recall that $P(E)$, which according to Eq. (5) defines the $I(V)$ and hence the $dI/dV(V)$ spectra of the Josephson junction, depends on T_{env} rather than $T_{T,S}$[32,33]. Thus, the absent temperature broadening indicates that T_{env} is decoupled from $T_{T,S}$. Indeed a situation were $T_{env} \gg T_{T,S}$ could naturally be realized due to an insufficient radiation shielding of the junction from the higher temperature stages of the cryostat[34,35].

To test the plausibility of the $T_{env} \gg T_{T,S}$ scenario, we used the $P(E)$ theory to fit the experimental $I(V)$ curve acquired simultaneously with the lowest temperature $dI/dV(V)$ spectrum from Fig. 3 recorded at $T_{ADR} = 34$ mK. As Fig. 4 shows, presumably due to the finite size effects in our superconducting tip, we registered a considerable quasiparticle tunneling background in the $I(V)$ data. To keep the number of fitting parameters small, we simply neglected the presence of the quasiparticle background, by constraining the fitting to the $[-25,25]$ μV interval of the bias voltage.

According to Eqs. (5), (8), (10)–(13), in the simplest case where the effective impedance of the circuit can be set to a real value R_{env}, the simulation of the experimental $I(V)$ data from Fig. 4 needs four fit parameters: C, R_{env}, E_J, and T_{env}. Making an unconstrained fit with these parameters is, however, impossible since C and T_{env} are coupled to each other, as can be seen in Eq. (12), which is expressed in terms of the ratio T/C. Therefore, we fix $C = 100$ fF in accordance with the BEM simulations of the STM junction discussed above, while freely varying the remaining three parameters R_{env}, E_J, and T_{env}. Note that, in principle, E_J could be obtained from the experimental data using the Ambegaokar–Baratoff formula[27,36]. However, here we used E_J as a fit parameter, because our data did not yield a reliable estimate of the superconducting gap Δ_T in the tip, necessary for the evaluation of E_J.

Figure 4 exhibits the experimental $I(V)$ spectrum of the Josephson junction measured at 34 mK (black curve). The curve clearly demonstrates the signature of the Josephson super current in the presence of thermal fluctuations in the environment[37]. We fit the experimental curve by calculating the $P(E)$ function according to the numerical procedure proposed by Ingold and Grabert[38] and also used by Ast and coworkers[26]. The fit (red curve) yields
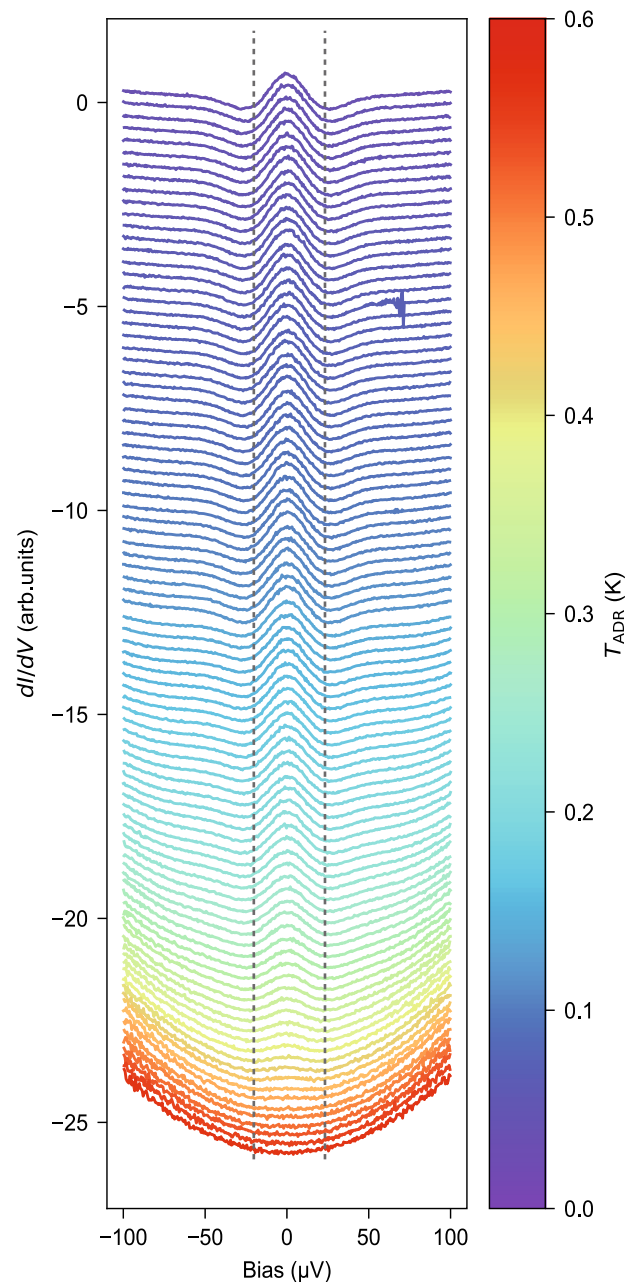

Fig. 3 Dependence of the differential conductance dI/dV of the Josephson junction on the cryostat temperature T_{ADR}. Higher-temperature data are shifted downwards for clarity. The dotted lines are guides to the eye, highlighting the temperature dependence of the Josephson conductance peak.

$T_{env} = 1.5$ K, $R_{env} = 31$ Ω and $E_J = 8$ μeV. The $P(E)$ function corresponding to the fit is shown in Fig. 5. The value of T_{env} obtained from the fit indicates that the scenario in which a cold mK STM junction is located inside a much warmer environment is indeed feasible. One could even speculate that the obtained value of T_{env} indicates the presence of thermal radiation from the 1 K stage of the cryostat. To visualize the effect that the environment has on the tunneling, we plotted in Fig. 4 another $I(V)$ (blue dashed) curve simulated with $T_{env} = 0.1$ K, i.e., for the case of a well-shielded junction with $T_{env} \approx T_{T,S}$. Figure 4 shows that a better shielding of the junction from the hot radiation could improve the spectroscopic resolution considerably.
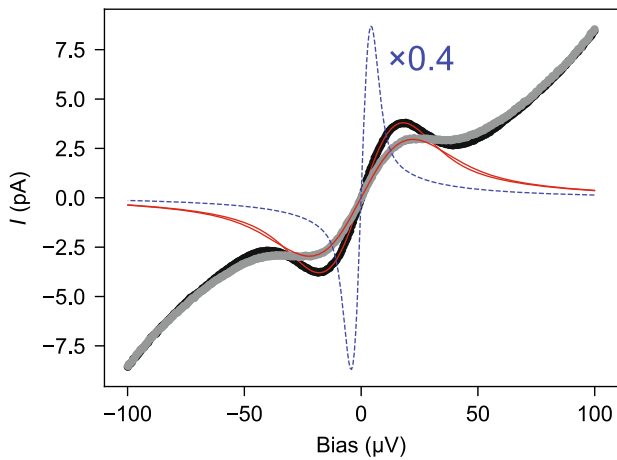
Fig. 4 The lowest temperature Josephson current spectra fitted using the $P(E)$ theory[26]. The black data series depicts the Josephson current $I(V)$ spectrum acquired simultaneously with the lowest temperature differential conductance dI/dV curve in Fig. 3 measured at 34 mK and fitted with the temperature of the environment $T_{env} = 1.5$ K (red curve, cf. text). Measured by the positions of the $I(V)$ extrema in this curve, the broadening due to environmental effects is 35 μV. The blue dashed line shows the $I(V)$ spectrum of a junction in a well-thermalized environment obtained with the same parameters as for the black curve (cf. text) but $T_{env} = 0.1$ K. The corresponding value of environmental broadening is 9 μV. Gray data correspond to the $I(V)$ spectrum of the Josephson junction measured at 34 mK with the high-frequency filter of the bias line[12] unplugged. The data were fitted with $T_{env} = 2.3$ K, keeping all other parameters unchanged (cf. text). Measured by the positions of the $I(V)$ extrema in this curve, the broadening due to environmental effects is 44 μV.
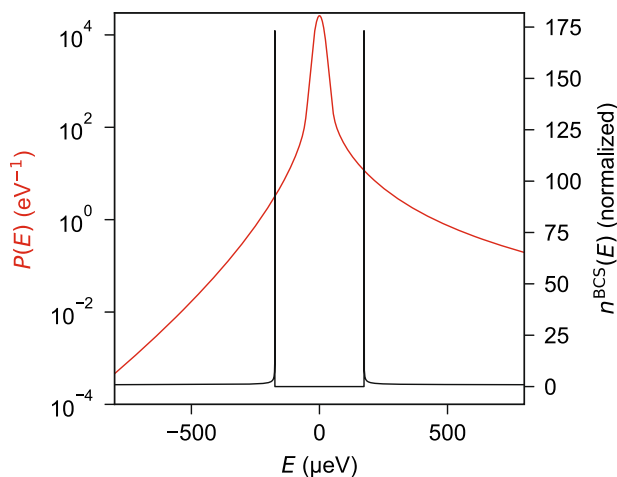

Fig. 5 The environmental $P(E)$ function[26]. The $P(E)$ function (red line) calculated for the temperature of the environment $T_{env} = 1.5$ K, environmental impedance $R_{env} = 31\Omega$, Josephson energy $E_J = 8$ μeV and junction capacitance $C = 100$ fF. The black curve displays the model density of states of a Bardeen–Cooper–Schrieffer (BCS) superconductor $n^{BCS}(E)$ calculated with the superconducting gap parameter $\Delta = 173$ μeV. The height of the quasiparticle peaks is limited by the finite size of the energy scale used in the calculation.

The thermal radiation arriving from the hotter stages of the cryostat affects the tunneling by coupling to the junction via its electrodes acting like an antenna[26]. However, the high-frequency noise from the room temperature electronics should also couple to the junction, producing an effective increase of T_{env}. We exploited a convenient possibility to demonstrate this effect

experimentally and re-measured the $I(V)$ spectrum of the Josephson junction at $T_{ADR} = 34$ mK with the Pi-filter of the bias line (see Methods section) unplugged. The spectrum measured without the filter shown as the gray curve in Fig. 4 was fitted with $T_{env} = 2.3$ K, keeping all other parameters fixed. Thus, unplugging the filter changes T_{env} and worsens the experimental resolution from 35 to 44 μV, as measured by the extrema of the Josephson current feature in Fig. 4.

We conclude the analysis of T_{env} by discussing its dependence on C. Varying C in the range between 50 and 150 fF, we find that $T_{env}(C) = C \,[\text{fF}] \times 16\,[\text{mK/fF}] - 70\,[\text{mK}]$. Thus T_{env} depends relatively weakly on C. The fact that T_{env} comes out close to the temperature of our 1K pot[12] generally supports the validity of our conclusions. The fact that T_{env} is not precisely 1 K could mean that our initial estimate of $C = 100$ fF may be too high, with the value of 70 fF being a more accurate estimate. At the same time, $T_{env} = 4$ K would demand $C = 250$ fF. We, however, can rule out this scenario because the broadening caused by the $P(E)$ function[26] calculated with these parameters makes fitting the superconducting gap spectra (see below) impossible.

Temperature of the tip. Having determined the influence of the junction environment, we now turn to the problem of estimating $T_{T,S}$, which, as was mentioned above, are the temperatures appearing in the Fermi-Dirac distributions of the tip and the sample electrodes. Generally speaking, the tip and the sample can have different temperatures, i.e., $T_T \neq T_S$. Therefore, to fully characterize the junction temperature, it could be necessary to perform two different experiments. As mentioned above, T_S can be obtained by STS with a superconducting tip on a normal-metal sample, while T_T follows from STS with a normal-metal tip on a superconducting sample. Assuming that the tip should have a higher temperature in our STM design, we only evaluate T_T as the upper bound on the junction temperature.

We remark that despite a consensus about the utility of $n^{BCS}(E)$ for estimating the junction temperature, there is no general agreement on the details of the analysis, with most variations occurring at the stage of fitting the experimental data. The problem is that using Eqs. (3) and (4) does not usually produce satisfactory fits, and as a consequence one has to employ expressions for the superconducting DOS that include additional parameters. The most commonly used expression of that type[3,5–10,12] was introduced by Dynes et al.[39] to account for the finite quasiparticle lifetime in a superconductor. It follows from Eq. (3) by introducing a phenomenological parameter γ

$$n_S^D = \text{Re}\left[\frac{E - i\gamma}{\sqrt{(E - i\gamma)^2 - \Delta^2}}\right]. \quad (6)$$

Although n_S^D indeed results in better fits of the STS data, the physical significance of γ remains unclear, which makes the fitting procedure ambiguous.

Besides the Dynes expression in Eq. (6), there have been attempts to fit the experimental STS of superconducting gaps with the so-called Maki formula, which considers the effects of magnetic scattering[5,7]. Inspection of the original work of Maki[40] reveals, however, that their approach applies to dirty super-conductors, for which the mean free path of an electron is smaller than the coherence length of a Cooper pair. Because our clean single-crystal Al(100) sample does not fulfill this condition, we only analyze our data using the Dynes expression in Eq. (6).

In Fig. 6a, we present a dI/dV spectrum of the superconducting gap measured on Al(100) with a normal-metal PtIr tip at $T_{ADR} = 44$ mK. As expected for this temperature, the curve features a fully developed superconducting gap and two sharp
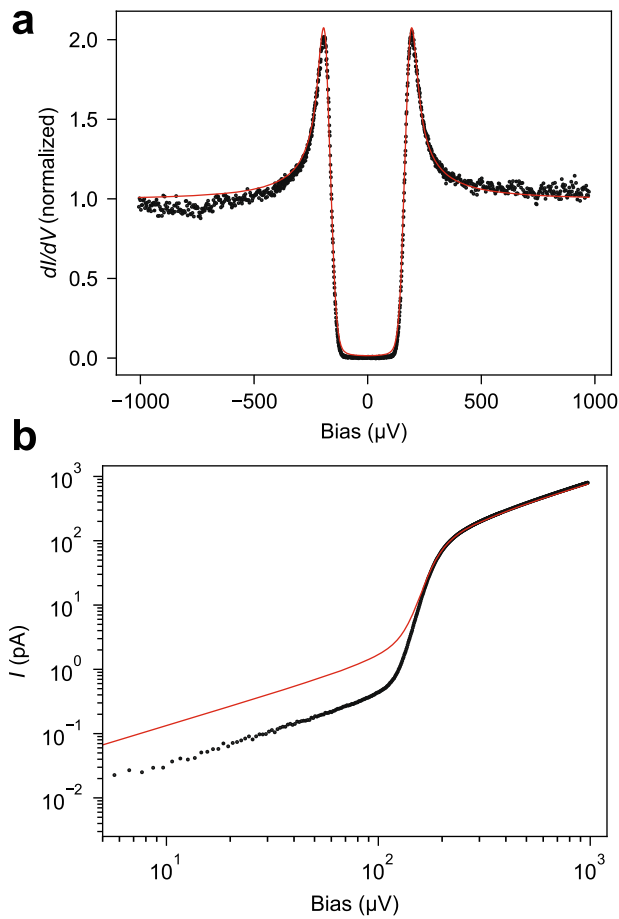
Fig. 6 Fitting the experimental differential conductance dI/dV spectrum of the superconducting gap. a Raw dI/dV spectrum of the superconducting Al(100) surface measured with a normal-metal tip at 44 mK and fitted with Eq. (4), where the model density of states of a Bardeen-Cooper-Schrieffer (BCS) superconductor n_S^{BCS} was substituted by the Dynes expression n_S^D defined in Eq. (6). For values of the fit parameters, cf. text. **b** The $I(V)$ curve (black dots) measured simultaneously with the dI/dV spectrum of panel (a) and fitted (red line) using the same parameter set used for calculating the fit in **a**, but complemented by the high-voltage or normal-state resistance of the junction, $R = 1.2$ MΩ.

conductance spikes situated symmetrically around zero bias. Following the standard approach, we fit the spectrum with Eq. (4) in which we substitute n_{BCS} with n_S^D and use Δ and γ (see Eq. (6)) as two independent fit parameters, while the Fermi–Dirac distribution in Eq. (4) contributes T_T as the third fit parameter. The $P(E)$ function in Eq. (4) introduces no additional fit parameters, as it is calculated with the fixed set of parameters determined earlier from the Josephson junction data analysis. Note that in using Eq. (4) we neglect the small effect of the 4 μV lock-in bias modulation (see "Methods").

Figure 6a shows the fit of the superconducting gap obtained with $\Delta = 175$ μeV, $\gamma = 2.4$ μeV, and $T_T = 99$ mK. Notice that the value of T_T comes out substantially lower than the one we reported earlier[12], which occurs mostly due to the inclusion of the $P(E)$ broadening effect into the consideration. The conventional fitting approach stops here, without giving detailed attention to the value of $\gamma = 2.4$ μeV, which seems to be an order of magnitude too high, if compared, e.g., to the data reported for mesoscopic junctions[41].

However, the unusually high γ causes a problem manifesting itself as a high zero-bias conductance visible by closer inspection
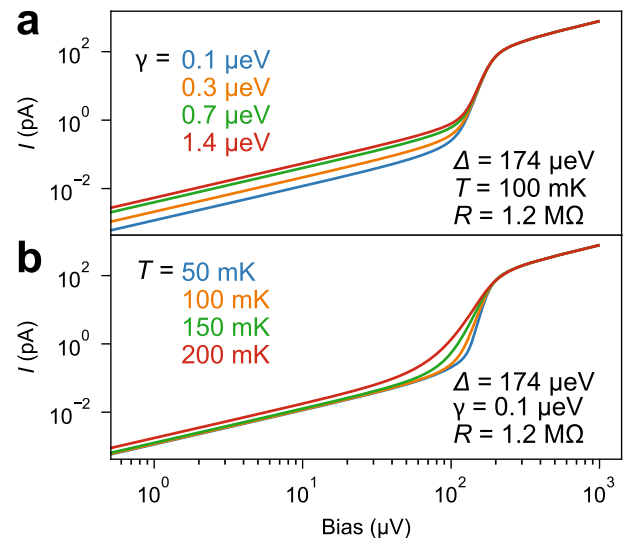

Fig. 7 Influence of the temperature T and the Dynes parameter γ on $I(V)$ curves simulated using the Dynes expression Eq. (6). a The $I(V)$ curves obtained by varying γ. **b** The $I(V)$ curves obtained by varying T. The values of the respective parameters are listed in the legend of each panel. R stands for the high-voltage or normal-state resistance of the junction. Δ is the superconducting gap parameter.

of the fit in Fig. 6a. Technically, the problem arises because the least-square fitting routine minimizes the total sum of *absolute* quadratic deviations $\sum_i \sqrt{x_i^2 - y_i^2}$ between the data x_i and the fit y_i calculated at every experimental point i. Because the minimized deviation is *absolute*, the points where the x_i are large contribute more to its sum. Conversely, the points inside the gap, where the x_i are small, produce a smaller contribution; hence, the deviations between the fit and the data inside the gap are less significant for minimizing that sum.

To exhibit the extent of the problem clearly, we show in Fig. 6b a log–log plot of the $I(V)$ curve measured simultaneously with the dI/dV data in Fig. 6a. The latter was fitted with a curve that has been generated with the same parameters as in Fig. 6a, but complemented with the high-voltage (i.e., normal-state) resistance $R = 1.2$ MΩ of the junction. Figure 6b confirms that the fitting of the experimental data inside the gap needs improvement.

Before we fix the problem with the fitting, it is instructive to inspect how the Dynes-generated $I(V)$ curve responds to changes in the parameters γ and T. Figure 7a shows that for small T and γ, the value of γ defines primarily the zero-bias conductance $G_{V=0}$ of the junction. T, on the other hand, as Fig. 7b shows, controls the sharpness of the transition between the low and high conductance regimes. Interestingly, as T increases, it smears the gap edge towards zero bias and thus also raises $G_{V=0}$. Comparing Fig. 6b and Fig. 7a, b, we see that the value of γ that we obtained from the standard fitting approach is indeed too high.

To fit the low energy part of the spectrum better, we change to fitting $I(V)$ instead of dI/dV curves. Besides that, we minimize the sum of *relative* quadratic deviations $\sum_i \sqrt{\left(\frac{x_i - y_i}{x_i + y_i}\right)^2}$. The modified fit obtained with $\Delta = 173$ μeV, $\gamma = 0.5$ μeV, $T_T = 78$ mK and $R_T = 1.2$ MΩ in Fig. 8a (red curve) exhibits a much better agreement in the gap. Nevertheless, the improvement in the gap comes at the expense of the fit quality at the quasiparticle peaks, where, as the inset of Fig. 8b shows, the new fit overshoots the experiment appreciably.

Concluding that the Dynes-generated curves cannot simultaneously fit all the features of the experimental superconducting
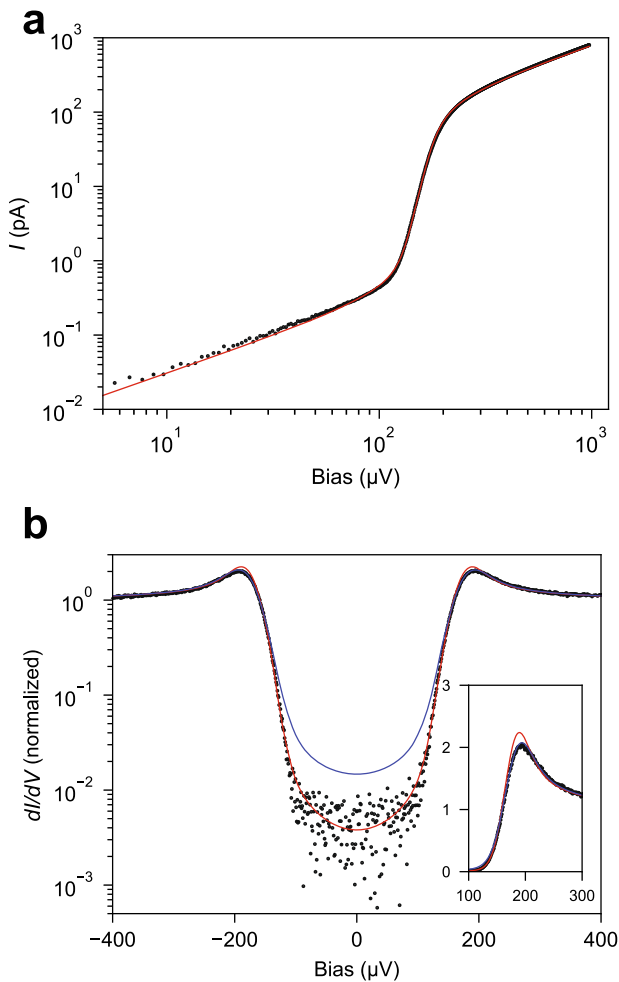
Fig. 8 Fitting the experimental $I(V)$ spectrum of the superconducting gap with the modified routine. a Fit of the $I(V)$ curve from Fig. 6b, achieved with the modified fitting routine (cf. text). **b** Differential conductance dI/dV spectrum corresponding to the $I(V)$ curve of **a**, plotted on a logarithmic scale to expose the quality of the fit in the low conductance regime. The red curve is generated with the same parameter set as in **a**. The blue curve is the fit from Fig. 6a. Quasiparticle peak feature plotted on a linear scale (inset).

gap spectrum, we come to the question of which part is more relevant for our analysis. We propose that the lower energy part of the spectrum lying below the quasiparticle peaks reflects the equilibrium properties of the junction better, because the measurement of the quasiparticle peaks occurs at a substantially higher current. Thus, as was also recently suggested by Schwenk et al.[11], the quasiparticle peaks may experience an additional non-intrinsic energy-dependent broadening. One could further speculate that the observed broadening may stem from non-equilibrium effects in the junction, e.g., local heating of the tip by the current of tunneling electrons[42]. If this indeed was the case, the temperature increase due to such heating could be about 20 mK, as Fig. 8b suggests.

Developing the argument further and recalling Fig. 7b, which shows how the zero-bias conductance $G_{V=0}(T)$ reacts to the increasing temperature, we wonder whether $G_{V=0}(T)$ alone could provide a good estimate of the temperature in the tip. To explore this question, we measured the junction characteristics, varying T_{ADR} between 44 mK and 1.2 K. As expected, the data plotted in Fig. 9a, b clearly show a gradual disappearance of the super-conducting gap upon increasing T_{ADR}. The experimental

$G_{V=0}(T_{ADR})$ plot in Fig. 10a extracted from the data in Fig. 9 reveals two regimes: Below $T_{ADR} \sim 200$ mK, $G_{V=0}$ stays almost constant, with its value determined by γ. At higher T_{ADR}, $G_{V=0}$ increases quickly, indicating that the smearing of the gap reaches zero bias, similar to Fig. 7b.

To simulate the $G_{V=0}(T_{ADR})$ curve with Eq. (6), we assumed that γ is independent of the temperature and used the value $\gamma = 0.5\,\mu$eV. Further, we calculated $\Delta(T)$ according to a well-known analytic formula[43] by taking the critical temperature T_c of Al to be 1.2 K and using $\Delta(T=0) = 173\,\mu$eV as obtained from the fit in Fig. 8a. Plotting the calculated $G_{V=0}(T)$ curve (red) in Fig. 10a next to the experiment, we find a striking agreement between both curves if the experimental temperature scale T_{ADR} is shifted by $T_{shift} = 45$ mK towards higher temperatures.

The data from Fig. 10a can be also plotted to show a T_{shift} for each individual experimental data point, which results in the $T_{shift}(T_{ADR})$ curve plotted in Fig. 10b. Apparently, our $G_{V=0}(T)$ analysis yields a reasonably precise estimate of T_{shift} in the range where $T_{ADR} \gtrsim 200$ mK. Due to the flattening of the $G_{V=0}(T)$ curve, however, the precision for $T_{ADR} < 200$ mK deteriorates, but it seems that one could nevertheless safely assume that T_{shift} remains roughly constant towards lower-temperatures. Interestingly, as T_{ADR} increases, T_{shift} tends to diminish, which could happen due to increasing heat conductivity of the materials, leading to a better thermalization of the tip.

Looking back at Fig. 8 that displays the $I(V)$ curve measured at $T_{ADR} = 44$ mK and recalling that $T_T = 78$ mK extracted from its fit, we can now compare this latter temperature to the $T_T = T_{ADR} + T_{shift} = 44$ mK + 45 mK = 89 mK predicted by the analysis of $G_{V=0}(T)$. It is noticeable that both values are well below the temperature of 99 mK obtained from the traditional fitting approach used in Fig. 6. Although the $G_{V=0}(T)$ approach may suffer from the reduced accuracy below 200 mK, at elevated temperatures it provides data with more confidence. Besides that, the dependence of the T_{shift} on T_{ADR} obtained by the $G_{V=0}(T)$ approach, may additionally reveal the physical origin of T_{shift}. All of this, to our opinion, makes the $G_{V=0}(T)$ approach into a useful complimentary tool for identifying the correct temperature of the mK STM junction.

Finally, we conclude our analysis by discussing γ, the microscopic origin of which, especially for temperatures far below T_c, is not yet well-understood. Recently, Pekkola et al.[41] proposed that γ may reflect the strength of photon-assisted tunneling that occurs at energies far below the gap edge. Assuming that our environment has a blackbody spectrum with $T_{env} = 1.5$ K, we obtain $2.7 \times T_{env} = 4.25$ K as the average energy of a photon. This is substantially higher than $\Delta/k_B \approx 2$ K, which points towards the possibility of photon assisted tunneling.

According to Eqs. (6) and (4) the dimensionless parameter γ/Δ is directly related to the ratio of the junction conductance at zero bias to its conductance at high bias, $\gamma/\Delta \simeq R/R_0$. Due to the presence of the superconducting gap, tunneling at zero bias can only occur if an electron absorbs energy larger than Δ from the environment. Because the probability of such an event is defined by the $P(E)$ function for $E \leq -\Delta$, Di Marco et al.[44] proposed to evaluate γ/Δ as

$$\gamma/\Delta \simeq 2 \int_{-\infty}^{-\Delta} dE\, n^{BCS}(E) P(E), \tag{7}$$

Using the parameters determined previously (by fitting to experimental data, see above), the two functions under the integral in Eq. (7) are plotted in Fig. 5. Evaluating the integral numerically yields $\gamma/\Delta = 4 \times 10^{-4}$, while the experimental fit in Fig. 8 provides $\gamma/\Delta = 3 \times 10^{-3}$. Taking the phenomenological character of the theory used to obtain the environmental $P(E)$
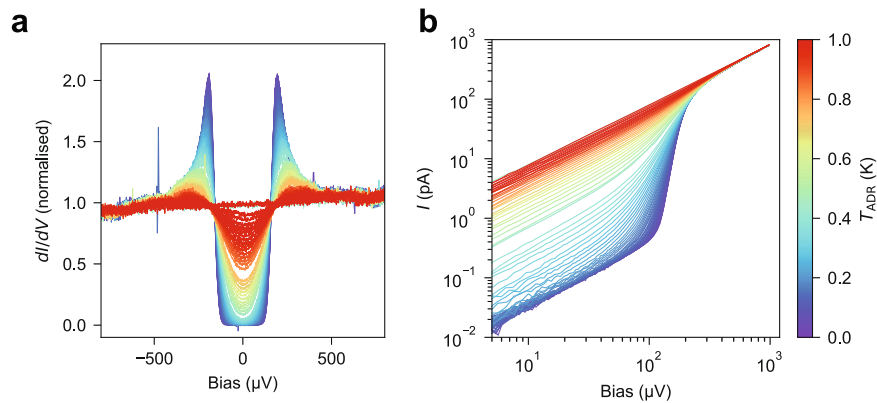
Fig. 9 Dependence of the experimental differential conductance dI/dV and $I(V)$ spectra of the normal-metal superconductor tunneling junction on the cryostat temperature T_{ADR}. a dI/dV spectra. **b** $I(V)$ spectra. The data were measured in a fully automatic mode, taking a spectrum every 30 min during approximately 48 h. The noise visible in the dI/dV data comes from the few curves that were affected by small instabilities of the junction, caused by rapid pressure variations in the helium exhaust line.
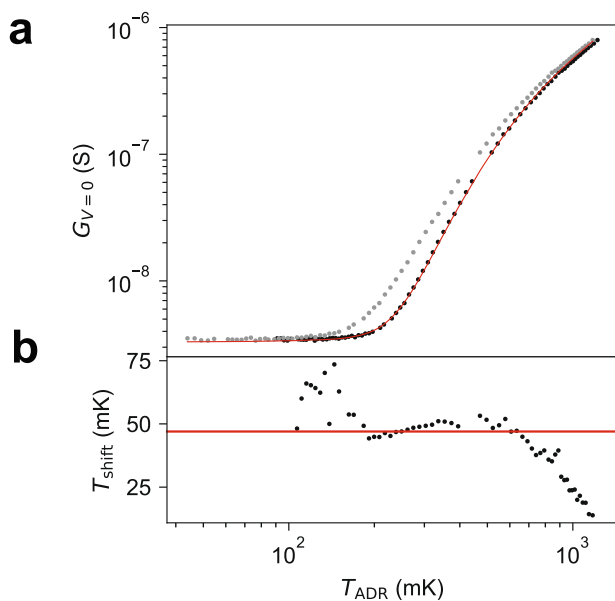

Fig. 10 Dependence of the zero-bias conductance $G_{V=0}$ of the normal-metal superconductor tunneling junction on the cryostat temperature T_{ADR}. a Thermal dependence of the zero-bias conductance $G_{V=0}$ obtained from the experiment (gray dots) and simulated (red line). The black dots are the same data but shifted rigidly by 45 mK to higher temperatures. **b** A temperature-dependent shift necessary for matching the experimental and simulated values of $G_{V=0}$ shown in **a**. Red horizontal line marks the value $T_{shift} = 45$ mK.

function, this result supports the idea of Pekola et al.[41] that the γ of the Dynes fit reflects the strength of photon-assisted tunneling. More explicit confirmation needs further experiments to measure the superconducting gap while systematically varying T_{env}.

In conclusion, our temperature-dependent STS data acquired with the Al/vacuum/Al(100) Josephson junction between 30 and 600 mK demonstrated no appreciable thermal broadening effects. We propose that this occurs due to the difference between the temperature T_{env} of the environment and the junction temperature $T_{T,S}$ with $T_{env} \gg T_{T,S}$. Fitting the Josephson STS data, we obtained the $P(E)$ function that characterizes the probability of the energy exchange between the environment and the junction. According to the fit, the temperature of the junction's environment is $T_{env} = 1.5$ K, substantially higher than the temperature of the ADR cryostat in which we performed the measurement.

Although our data provide a qualitatively clear picture of a cold STM junction embedded in a hot environment, the obtained value of T_{env} needs to be treated with caution, due to the phenomenological character of the approach to calculating the $P(E)$ function and the crudeness with which we evaluated the junction capacitance C.

Using the tunneling spectrum of the superconducting gap measured with a normal-metal tip on the Al(100) surface, we have demonstrated the potential fallibility of the usual dI/dV fitting, which does not pay sufficient attention to the range of data found below the quasiparticle peaks. We showed that minimizing the relative deviation helps achieving a much better fit of the spectral range below the quasiparticle peaks, albeit at the expense of the fit quality of the quasiparticle peaks. However, as we argued, the quasiparticle peaks may be subject to additional non-intrinsic and energy-dependent broadening mechanisms. Therefore, their accurate fitting may not be necessary for determining the intrinsic parameters such as the junction's temperature and the Dynes γ. Using a modified fitting routine, we found that at $T_{ADR} = 44$ mK the Fermi-Dirac distribution temperature in the tip was $T_T = 77$ mK and $\gamma = 0.5$ μeV or $\gamma/\Delta = 0.003$.

We also proposed a new way of determining the temperature of the STM junction by analyzing the temperature scaling of the zero-bias conductance $G_{V=0}(T)$ only. Using this approach, we reconstructed T_T by mapping out its deviation T_{shift} from the cryostat temperature T_{ADR}. Our data showed that $T_{shift} \approx 45$ mK for $T < 600$ mK. According to this method, the lowest T_T that we can currently achieve in our setup is 26 mK + 45 mK = 71 mK.

Finally, our data suggest that the value of the Dynes parameter γ obtained from fitting the superconducting gap, in agreement with the proposal of Pekkola et al.[41,44], reflects the strength of photon-assisted tunneling caused by the radiation arriving at the STM junction from the hotter stages of the cryostat. This finding emphasizes the importance of good radiation shielding and possibly low-temperature high-frequency filtering in the design of a mK STM.

Methods
Experimental setup. We performed the experiments in a mK STM, the details and performance of which were reported recently[12]. Thus, we only briefly list its essential characteristics here. The STM head is thermally well-anchored to a base plate of an adiabatic demagnetization refrigerator (ADR) that resides inside a UHV chamber. The ADR reaches a minimum temperature of 26 mK, measured by a calibrated ruthenium oxide sensor positioned on the base plate of the ADR right next to the STM head. We refer to the temperature reading of that thermometer as T_{ADR}. ADR enables STM/STS experiments at varying T_{ADR} spanning the range between 30 mK and 1–2 K. STM/STS can be performed in the presence of a

magnetic field of up to 8 T applied in the direction perpendicular to the sample surface. To reduce the high-frequency noise in the junction we use Pi-filters on the bias and all five high-voltage piezo lines.

Scanning tunneling spectroscopy (STS). The STS data discussed here were acquired on the clean surface of an Al(100) single crystal clamped to a custom-made flag-type sample holder. The sample holder body was fabricated from tungsten, while the clamping comprised a molybdenum foil and a set of molybdenum screws fixing the foil to the sample holder body. Due to the superconductivity of molybdenum, we made sure that the foil contained no closed holes to prevent flux trapping at low temperatures. The sample surface was prepared in UHV by repeated cycles of Ar^+ ion sputtering and subsequent annealing at 400 °C. We used low-energy electron diffraction (LEED) and Auger electron spectroscopy (AES) to verify the surface quality.

The Al(100) sample was superconducting during all of the STS measurements reported here. Interestingly, we could only observe the superconductivity by applying a compensating B field of 8–10 mT to the sample magnet. We speculate that the compensation field was necessary to neutralize the effect of the magnetic flux caught by one of the superconducting coils during the ADR run[12].

The superconductivity in the sample always appeared abruptly upon ramping up the compensating B field. Moreover, the tunneling spectrum of the superconducting gap did not change when the compensating sample B field was further varied. Instead, it disappeared and reappeared erratically. We rationalize this behavior by assuming that our sample was mainly in an intermediate state characterized by an ordered structure of macroscopically large superconducting domains separated by normal-metal areas[24]. In such a state, slight variations of the sample B field can cause rearrangements of the domain structure, which, in turn, produce abrupt changes in the type of the domain (superconducting vs. normal) faced by the tip.

The Josephson junction STS data were measured at 30 mK $\leq T_{ADR} \leq$ 600 mK with a compensating field of 8 mT kept throughout the measurement series. For the measurement, the PtIr tip was made superconducting by indenting it gently into the Al(100) surface until the Josephson conductance peak at zero bias (see Fig. 3) appeared in the conductance spectra. The series of spectra featuring the superconducting gap of the Al(100) surface (Fig. 9) was acquired with a clean PtIr tip at 40 mK $\leq T_{ADR} \leq$ 1.2 K. The lower temperature data were collected with the compensating field of 8 mT. At $T_{ADR} \approx$ 460 mK, the sample superconductivity disappeared abruptly, and we regained it by tuning the compensating field to 10 mT, the value at which all higher temperature data were then collected.

STS was performed using the internal lock-in of the Nanonis software. The parameters of the lock-in were: modulation frequency 187.7 Hz, modulation amplitude 2 μV for the Josephson (Fig. 3) and 4 μV for the superconducting gap spectroscopy (Fig. 9). The tunneling current was measured using a fixed gain (10^{10}) amplifier from NF Corporation[12]. All experimental data are displayed as raw data without any additional postprocessing. Each presented STS curve is a single-sweep spectrum acquired in less than 220 s.

Fitting STS data with the P(E) theory. The $P(E)$ theory, which was originally developed for mesoscopic tunneling junctions[20], derives the $P(E)$ function from the junction's equilibrium phase-phase correlation function $J(t) \equiv \langle [\tilde{\phi}(t) - \tilde{\phi}(0)]\tilde{\phi}(t) \rangle$,

$$P(E) = \frac{1}{2\pi\hbar} \int_{-\infty}^{\infty} dt \, \exp\left[J(t) + \frac{i}{\hbar} Et \right]. \tag{8}$$

According to the Wiener–Khinchin theorem (see Appendix of Clerk et al.[45]), $P(E)$ is a noise power spectral density of the junction's charge shift operator $\exp(-i\tilde{\phi})$, where the phase $\tilde{\phi}(t)$ is defined as

$$\tilde{\phi}(t) = \frac{e}{\hbar} \left(\int_{-\infty}^{t} dt' \, U(t') - Vt \right), \tag{9}$$

with $U = Q/C$ being the momentary voltage across the junction with capacitance C charged by Q, and V is the constant voltage applied by an external source considered to be ideal.

In their pioneering attempt to apply the $P(E)$ theory to the STM, Ast and coworkers extended the theory by pointing out that the fluctuations of the phase seen by the STM junction split into two contributions[26]: $J(t) = J_0(t) + J_N(t)$. According to the fluctuation-dissipation theorem, $J_0(t)$ is related to the imaginary part of the response function $\chi(\omega) = (e/\hbar)^2 Z_t(\omega)/i\omega$, where $Z_t(\omega)$ is the total impedance of the circuit consisting of the the junction capacitance C and the environmental impedance $Z(\omega)$, via[20]

$$
\begin{aligned}
J_0(t) = \quad & 2 \int_0^{\infty} \frac{d\omega}{\omega} \frac{\text{Re}[Z_t(\omega)]}{R_K} \times \\
& \left[\coth\left(\frac{1}{2} \frac{\hbar\omega}{k_B T} \right)[\cos(\omega t) - 1] - i\sin(\omega t) \right].
\end{aligned}
\tag{10}
$$

The newly introduced term $J_N(t)$ determines thermal voltage noise on the junction capacitor C. Splitting $J(t)$ into the two contributions helps expressing the $P(E)$ function as a convolution of two parts

$$P(E) = \int_{-\infty}^{+\infty} dE' P_0(E - E') P_N(E'), \tag{11}$$

where P_N is related to $J_N(t)$ and takes a simple Gaussian form

$$P_N(E) = \frac{1}{\sqrt{4\pi E_C k_B T}} \exp\left[-\frac{E^2}{4E_C k_B T} \right], \tag{12}$$

with $E_C = e^2/2C$ being the charging energy of the STM junction capacitor C. Note that for the Josephson current carried by Cooper pairs $E_C = (2e)^2/2C$.

According to Eqs. (10) and (12), both $P_0(E)$ and $P_N(E)$ depend on the temperature of the junction environment T_{env}[32]. Therefore, calculating $P(E)$ and using it in Eq. (5) for fitting the experimental $I(V)$ characteristics of a Josephson junction should yield T_{env}.

While obtaining $P_N(E)$ is straightforward, the calculation of $P_0(E)$, according to Eq. (10), becomes a task of finding $Z_t(\omega)$. Currently, there are no well-established schemes which allow doing this reliably for the case of an STM junction. Therefore, we follow the procedure developed for mesoscopic tunneling junctions[20,26]. That approach starts by representing the junction and its environment as a lumped-element circuit with the tunneling junction shunted by a capacitance C and connected to an ideal voltage source via an environmental impedance $Z(\omega)$. Then, the expression for $Z_t(\omega)$ can be written as[20]

$$Z_t(\omega) = \frac{1}{i\omega C + 1/Z(\omega)}. \tag{13}$$

In the simplest case, $Z(\omega)$ only has a dissipative part that is independent of ω, i.e., $Z(\omega) = R_{env}$[20,35,41,44]. The value R_{env} determines the strength of coupling between the junction and its environment, with $R_{env} \ll R_Q \equiv h/e^2$ determining the weak coupling regime in which most tunneling electrons leave the environmental modes, except those close to $\omega = 0$, undisturbed, the $P(E)$ function is thus peaked at $E = 0$, and the charge transferred through the junction is removed almost instantaneously by the voltage source[20]. According to Eq. (5), fitting of the $I(V)$ curves measured with a Josephson junction then needs four fit parameters: C, R_{env}, E_J, and T_{env}.

Data availability
All data presented in this paper are publicly available through the Jülich Data repository with identifier https://doi.org/10.26165/JUELICH-DATA/KKEXFT.

Code availability
The codes used to obtain the results of this work are available from the corresponding authors upon reasonable request.

References
1. Wagner, C. & Temirov, R. Tunnelling junctions with additional degrees of freedom: an extended toolbox of scanning probe microscopy. *Prog. Surf. Sci.* **90**, 194–222 (2015).
2. Chen, Y., Bae, Y. & Heinrich, A. J. Harnessing the quantum behavior of spins on surfaces. *Adv. Mater.* 2107534 (2022).
3. Song, Y. J. et al. Invited review article: a 10 mK scanning probe microscopy facility. *Rev. Sci. Instrum.* **81**, 121101 (2010).
4. Misra, S. et al. Design and performance of an ultra-high vacuum scanning tunneling microscope operating at dilution refrigerator temperatures and high magnetic fields. *Rev. Sci. Instrum.* **84**, 103903 (2013).
5. Assig, M. et al. A 10 mK scanning tunneling microscope operating in ultra high vacuum and high magnetic fields. *Rev. Sci. Instrum.* **84**, 033903 (2013).
6. Roychowdhury, A. et al. A 30 mK, 13.5 T scanning tunneling microscope with two independent tips. *Rev. Sci. Instrum.* **85**, 043706 (2014).
7. Machida, T., Kohsaka, Y. & Hanaguri, T. A scanning tunneling microscope for spectroscopic imaging below 90 mK in magnetic fields up to 17.5 T. *Rev. Sci. Instrum.* **89**, 093707 (2018).
8. Balashov, T., Meyer, M. & Wulfhekel, W. A compact ultrahigh vacuum scanning tunneling microscope with dilution refrigeration. *Rev. Sci. Instrum.* **89**, 113707 (2018).
9. von Allwörden, H. et al. Design and performance of an ultra-high vacuum spin-polarized scanning tunneling microscope operating at 30 mK and in a vector magnetic field. *Rev. Sci. Instrum.* **89**, 033902 (2018).
10. Wong, D. et al. A modular ultra-high vacuum millikelvin scanning tunneling microscope. *Rev. Sci. Instrum.* **91**, 023703 (2020).
11. Schwenk, J. et al. Achieving μeV tunneling resolution in an in-operando scanning tunneling microscopy, atomic force microscopy, and magnetotransport system for quantum materials research. *Rev. Sci. Instrum.* **91**, 071101 (2020).

12. Esat, T. et al. A millikelvin scanning tunneling microscope in ultra-high vacuum with adiabatic demagnetization refrigeration. *Rev. Sci. Instrum.* **92**, 063701 (2021).

13. Fernández-Lomana, M. et al. Millikelvin scanning tunneling microscope at 20/22 T with a graphite enabled stick-slip approach and an energy resolution below 8 μeV: application to conductance quantization at 20 T in single atom point contacts of Al and Au and to the charge density wave of 2H-NbSe₂. *Rev. Sci. Instrum.* **92**, 093701 (2021).

14. Machida, T. et al. Zero-energy vortex bound state in the superconducting topological surface state of Fe(Se,Te). *Nat. Mater.* **18**, 811–815 (2019).

15. Nuckolls, K. P. et al. Strongly correlated Chern insulators in magic-angle twisted bilayer graphene. *Nature* **588**, 610–615 (2020).

16. Kamber, U. et al. Self-induced spin glass state in elemental and crystalline neodymium. *Science* **368**, eaay6757 (2020).

17. Song, Y. J. et al. High-resolution tunnelling spectroscopy of a graphene quartet. *Nature* **467**, 185–189 (2010).

18. Yazdani, A., da Silva Neto, E. H. & Aynajian, P. Spectroscopic imaging of strongly correlated electronic states. *Annu. Rev. Condens. Matter Phys.* **7**, 11–33 (2016).

19. Feldman, B. E. et al. High-resolution studies of the Majorana atomic chain platform. *Nat. Phys.* **13**, 286–291 (2017).

20. Grabert, H. & Devoret, M. H. (eds.) *Single Charge Tunneling: Coulomb Blockade Phenomena in Nanostructures* (Plenum Press, 1992).

21. Bardeen, J. Tunnelling from a many-particle point of view. *Phys. Rev. Lett.* **6**, 57–59 (1961).

22. Voigtländer, B. *Scanning Probe Microscopy* (Springer Berlin Heidelberg, 2015).

23. Gottlieb, A. D. & Wesoloski, L. Bardeen's tunnelling theory as applied to scanning tunnelling microscopy: a technical guide to the traditional interpretation. *Nanotechnology* **17**, R57–R65 (2006).

24. Tinkham, M. *Introduction to Supeconductivity* (McGraw Hill, 1996).

25. Jäck, B. et al. A nanoscale gigahertz source realized with Josephson scanning tunneling microscopy. *Appl. Phys. Lett.* **106**, 013109 (2015).

26. Ast, C. R. et al. Sensing the quantum limit in scanning tunnelling spectroscopy. *Nat. Commun.* **7**, 13009 (2016).

27. Jäck, B. et al. Critical Josephson current in the dynamical Coulomb blockade regime. *Phys. Rev. B* **93**, 020504 (2016).

28. Jäck, B. et al. Quantum Brownian motion at strong dissipation probed by superconducting tunnel junctions. *Phys. Rev. Lett.* **119**, 147702 (2017).

29. Senkpiel, J. et al. Single channel Josephson effect in a high transmission atomic contact. *Commun. Phys.* **3**, 131 (2020).

30. Senkpiel, J. et al. Dynamical Coulomb blockade as a local probe for quantum transport. *Phys. Rev. Lett.* **124**, 156803 (2020).

31. Senkpiel, J. et al. Extracting transport channel transmissions in scanning tunneling microscopy using superconducting excess current. *Phys. Rev. B* **105**, 165401 (2022).

32. Martinis, J. M. & Nahum, M. Effect of environmental noise on the accuracy of Coulomb-blockade devices. *Phys. Rev. B* **48**, 18316–18319 (1993).

33. Siewert, J., Nazarov, Y. V. & Falci, G. A generalized model of non-thermal noise in the electromagnetic environment of small-capacitance tunnel junctions. *Europhys. Lett.* **38**, 365–370 (1997).

34. Hergenrother, J. M., Tuominen, M. T., Lu, J. G., Ralph, D. C. & Tinkham, M. Charge transport and photon-assisted tunneling in the NSN single-electron transistor. *Phys. B Condens. Matter* **203**, 327–339 (1994).

35. Hergenrother, J. M., Lu, J. G., Tuominen, M. T., Ralph, D. C. & Tinkham, M. Photon-activated switch behavior in the single-electron transistor with a superconducting island. *Phys. Rev. B* **51**, 9407–9410 (1995).

36. Ambegaokar, V. & Baratoff, A. Tunneling between superconductors. *Phys. Rev. Lett.* **11**, 104 (1963).

37. Joyez, P., Vion, D., Götz, M., Devoret, M. & Esteve, D. The Josephson effect in nanoscale tunnel junctions. *J. Supercond.* **12**, 757–766 (1999).

38. Ingold, G. L. & Grabert, H. Finite-temperature current-voltage characteristics of ultrasmall tunnel junctions. *Europhys. Lett.* **14**, 371–376 (1991).

39. Dynes, R. C., Narayanamurti, V. & Garno, J. P. Direct measurement of quasiparticle-lifetime broadening in a strong-coupled superconductor. *Phys. Rev. Lett.* **41**, 1509–1512 (1978).

40. Maki, K. Pauli paramagnetism and superconducting state. II. *Prog. Theor. Phys.* **32**, 29–36 (1964).

41. Pekola, J. P. et al. Environment-assisted tunneling as an origin of the Dynes density of states. *Phys. Rev. Lett.* **105**, 026803 (2010).

42. Nahum, M., Eiles, T. M. & Martinis, J. M. Electronic microrefrigerator based on a normal-insulator-superconductor tunnel junction. *Appl. Phys. Lett.* **65**, 3123–3125 (1994).

43. Gasparovic, R. F., Taylor, B. N. & Eck, R. E. Temperature dependence of the superconducting energy gap of Pb. *Solid State Commun.* **4**, 59–63 (1966).

44. Di Marco, A., Maisi, V. F., Pekola, J. P. & Hekking, F. W. J. Leakage current of a superconductor–normal metal tunnel junction connected to a high-temperature environment. *Phys. Rev. B* **88**, 174507 (2013).

45. Clerk, A. A., Devoret, M. H., Girvin, S. M., Marquardt, F. & Schoelkopf, R. J. Introduction to quantum noise, measurement, and amplification. *Rev. Mod. Phys.* **82**, 1155–1208 (2010).

Acknowledgements

Author contributions

T.E., F.S.T., and R.T. conceived the experiment. T.E. and R.T. performed the measurements with technical help from X.Y. and F.M. T.E. and R.T. analyzed the experimental data. H.S. performed the BEM calculations of the STM junction capacitance. R.T. wrote the manuscript with significant input from F.S.T. All authors discussed the results and reviewed the manuscript.

Funding

Competing interests

The authors declare no competing interests.

Additional information

Supplementary information The online version contains supplementary material available at https://doi.org/10.1038/s42005-023-01201-4.

Correspondence and requests for materials should be addressed to Ruslan Temirov.

Peer review information *Communications Physics* thanks Berthold Jaeck and the other, anonymous, reviewer(s) for their contribution to the peer review of this work. Peer reviewer reports are available.

Reprints and permission information is available at http://www.nature.com/reprints

Publisher's note Springer Nature remains neutral with regard to jurisdictional claims in published maps and institutional affiliations.